

Structural behavior of GFRP pultruded profiles reinforced with CFRP sheets

Experimental characterization and numerical modeling

Francisco Felício Nunes

Abstract: *In the last decades, GFRP (Glass Fiber Reinforced Polymer) pultruded profiles have been a growing segment of the construction industry, particularly in bridge deck construction. Despite all their advantages, the diversity of raw materials used to produce FRP pultruded parts leads to a high difficulty in establishing codes or guidelines for design. In this dissertation, the structural behavior of a prototype of GFRP hybrid pultruded profiles reinforced with CFRP (Carbon Fiber Reinforced Polymer) sheets on its flanges was studied. The mechanical properties of the material were obtained from coupon testing; specimens were extracted from the web and flanges of the profile. In a further stage, four short columns subjected to axial compression and one beam subjected to 4-point bending (and laterally braced) were tested. The structural behavior for serviceability and ultimate limit states of each type of structural element were analyzed, with particular attention being given to the ultimate limit state of local buckling. Along with the experimental characterization, the numerical modeling of the structural elements tested was developed using the ABAQUS software. Preliminary finite element method models (FEM) were developed using the mechanical properties obtained from coupon testing. Those models were calibrated based on the experimental structural element behavior and parametric studies were subsequently conducted.*

Keywords: *GFRP, CFRP, Local buckling, Pultruded profiles, Experimental tests, Numeric modeling.*

1. INTRODUCTION

A composite material is defined as a combination of two different materials, gathering in itself the best characteristics of each one. Nowadays, the most used composite material in construction industry is reinforced concrete; gathering the best qualities of steel (tensile strength) and concrete (compressive strength) [1]. In this dissertation, the structural behavior of FRP (Fiber Reinforced Polymer) pultruded profiles was studied.

Over the last decades, costs related to structural maintenance and reinforcement have been rising considerably. Moreover, there has been an even greater demand for faster construction [2]. Both these factors contributed to a significant boost of lighter and more durable materials. The FRP pultruded profiles are showing to be a competitive alternative in some niches of construction industry.

The FRP pultruded profiles are composite materials usually composed by glass fibers (GFRP) or carbon fibers (CFRP) embedded in a vinyl-ester or polyester matrix. The main advantages of its use are related to its high strength, reduced weight, electromagnetic transparency, durability and resistance to corrosive agents [3].

Despite all their referred advantages, the use of FRP pultruded profiles is still hindered by some limitations related to production costs, deformability, buckling sensitivity, connection technology, and the lack of design codes.

2. FOCUS AND DEVELOPED WORK

The main goal of the present dissertation is the study of the structural behavior of hybrid GFRP and CFRP pultruded profiles. All work and investigation presented was carried out to help the establishment of consensual design approaches. Also, the developed work contributed to the characterization of a prototype hybrid FRP pultruded profile produced by ALTO Perfis Pultrudidos Lda.

The present research may be divided in four different chronological stages:

- (i) Material mechanical characterization;
- (ii) Initial numerical FE models of the experimental tests;
- (iii) Experimental test of four short columns subjected to axial compression and one beam subjected to 4-point bending;
- (iv) Calibration of the initial numerical models according to the experimental results.

These stages are grouped in two main chapters: experimental characterization and numerical modeling.

The geometrical properties reported by the manufacturer are presented in Figure 1.

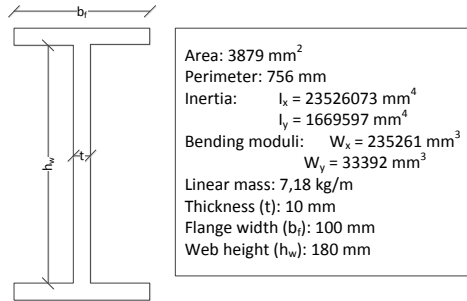


Figure 1. Geometrical properties of the studied profile

The nominal thickness of the CFRP sheet is 1,5 mm. Since the studied profile had a heterogeneous cross-section it was necessary to determine the effective shear area by analytical calculation (1606 mm^2). The reported fiber volume of the pultruded profile was $60 \pm 10\%$.

3. MECHANICAL CHARACTERIZATION

In order to obtain the mechanical properties of the studied material, such as strengths and elastic moduli, tests were carried out on specimens cut from the web and flanges of the studied profile. Specimens were cut and tested according to the ISO or ASTM standard test methods presented in Table 1. In the following sections some notes for each mechanical test are presented.

Table 1. Standard test methods used in mechanical characterization

Test	Standard
Bending	EN ISO 14125 [4]
Interlaminar shear	ASTM D 2344/D 2344M-00 [5]
Compression	ASTM D 695-02 [6]
Tension	ISO 527-4 [7]
In-plane Shear	ISO 527-5 [8]

3.1. BENDING TEST

Three-point bending tests (EN ISO 14125) were conducted on specimens with nominal dimensions of $300 \times 15 \times 10 \text{ mm}$, in order to determine the longitudinal elastic modulus in bending (E_f), the flexural strength (σ_{fu}) and the strain at failure (ϵ_{fu}) in the longitudinal direction. The tested span was 200 mm. The failure mode occurred with tensile failure of the lower face fibers as shown in Figure 2. Eight speci-

mens of each part (web or flanges) were tested. Four of the flange specimens were tested with the CFRP sheet on the upper face (CFRP_{sup}) and the remaining were tested with the CFRP sheet on the lower face (CFRP_{inf}). During the test of the CFRP_{sup} specimens, the delamination of the CFRP sheet was observed for an elongation of 0,62%.

3.2. INTERLAMINAR SHEAR TEST

Interlaminar shear tests (ASTM D 2344/D 2344M-00) were conducted on specimens with nominal dimensions of $60 \times 15 \times 10 \text{ mm}$ applying a concentrated load at the center of a 39 mm span, in order to determine the interlaminar shear strength (F^{sbs}). The failure mode occurred with interlaminar failure as shown in Figure 3. Four of the flange specimens were tested with the CFRP sheet on the upper face (CFRP_{sup}) and the remaining were tested with the CFRP sheet on the lower face (CFRP_{inf}).

3.3. COMPRESSIVE TEST

Compressive tests (ASTM D 695-02) were conducted on specimens with nominal dimensions of $40 \times 12,7 \times 10 \text{ mm}$ in the longitudinal direction and $30 \times 12,7 \times 10 \text{ mm}$ in the transverse direction, in order to determine the elastic modulus in compression (E_c), the compressive strength (σ_{cu}) and the strain at failure (ϵ_{cu}) for both directions. The failure mode occurred with material crushing and delamination as shown in Figure 4. The delamination of the CFRP sheet was observed for $\epsilon \approx 0,005$.

3.4. TENSILE TEST

Tensile tests (ISO 527-4) were conducted on specimens with nominal dimensions of $300 \times 25 \times 10 \text{ mm}$, in order to determine the elastic modulus in tension (E_t), the tensile strength (σ_{tu}) and the Poisson's ratio (ν_{xy}) in the longitudinal direction. The distance between the claws was 150 mm. The failure mode occurred with tensile failure of the fiber reinforcement as shown in Figure 5.

3.5. IN-PLANE SHEAR TEST

In-plane shear tests (10° off-axis) were conducted on specimens with $250 \times 25 \times 10 \text{ mm}$, in order to determine the shear modulus (G) and the in-plane shear strength (τ_u). The distance between the claws was 150 mm. The failure mode occurred with shear failure as shown in Figure 6. All the properties obtained in the mechanical characterization are presented in Tables 2 and 3.



Figure 2. Bending test failure



Figure 3. Interlaminar shear test failure



Figure 4. Compressive test failure



Figure 5. Tensile test failure



Figure 6. In-plane shear failure

Table 2. Summary of results for web specimens

Mechanical property / Test and direction	Bending		Compression		Tension
	Longitudinal	Longitudinal	Longitudinal	Transverse	Longitudinal
σ_u (MPa)	484,8 ± 11,2	495,1 ± 53,7	130,1 ± 11,67	396,6 ± 27,6	
E (GPa)	22,16 ± 1,57	26,16 ± 1,29	9,35 ± 0,61	32,81 ± 1,48	
ϵ_u (% m/m)	2,82 ± 0,23	2,51 ± 0,09	1,90 ± 0,20	-	
F^{sbs} (MPa)	31,33 ± 2,50				
τ_u (MPa)	30,59 ± 0,94				
ν_{xy}	0,266				
G (GPa)	3,73 ± 0,16				

Table 3. Summary of results for flange specimens

Mechanical property / Test and direction	Longitudinal bending		Compression		Tension
	CFRP _{sup}	CFRP _{inf}	Longitudinal	Transverse	Longitudinal
σ_u (MPa)	422,1 ± 25,0	620,4 ± 37,2	485,0 ± 23,6	92,3 ± 10,7	412,7 ± 16,1
E (GPa)	44,24 ± 7,70	48,13 ± 4,35	25,74 ± 2,66	10,15 ± 1,62	55,17 ± 3,11
ϵ_u (% m/m)	2,30 ± 0,30	1,50 ± 0,14	2,25 ± 0,17	1,52 ± 0,24	-
F^{sbs} (MPa)	31,70 ± 2,29				

4. SERVICEABILITY LIMIT STATES

4.1. AXIAL DEFLECTION

The use of the uniaxial bar theory is recommended by both the Structural Plastics Design Manual [9] and the Eurocomp Design Code and Handbook [10] to determine the deflection of pultruded compression members.

The axial shortening (ΔL) of a column under axial compression can be determined using the following equation,

$$\Delta L = \frac{PL}{E_L A} \quad (1)$$

where P is the applied load, L is the column length, E_L is the longitudinal elastic modulus and A is the cross-section area.

4.2. TRANSVERSE DEFLECTION

The use of the Timoshenko beam theory is recommended by both the Structural Plastics Design Manual [9] and the Eurocomp Design Code and Handbook [10] of pultruded axial members.

The deflection (δ) of a simply supported beam can be determined using the following equations,

$$\delta(z) = \frac{P}{EI} \left(\frac{z^3}{12} + \frac{(L-L_0)^2 z}{16} - \frac{L(L-L_0)z}{8} \right) - \frac{P}{KGA} \left(\frac{z}{2} \right) \quad (2)$$

$\rightarrow z < \frac{L-L_0}{2}$

$$\delta(z) = \frac{P}{EI} \left(\frac{(L-L_0)z^2}{8} - \frac{L(L-L_0)z}{8} + \frac{(L-L_0)^3}{96} \right) - \frac{P}{KGA} \left(\frac{(L-L_0)}{4} \right) \rightarrow z > \frac{L-L_0}{2} \quad (3)$$

where z is the distance to the beam end, P is the total applied load, L is the beam span, L_0 is the distance between load points, EI is the flexural rigidity and KGA is the shear rigidity.

5. ULTIMATE LIMIT STATE OF LOCAL BUCKLING

FRP pultruded profiles are particularly susceptible to local buckling under transverse loads due to the low in-plane moduli and the slenderness of the plate elements (web and flanges)[4]. Such phenomenon occurs both on columns or beams with a thin-walled cross section. Numerous experimental or numerical studies on the local buckling of FRP plate elements were carried out in recent years (Bank et al. [11], Mottram [12], Turvey and Zhang [13]). The typical failure mode of this ultimate limit state is the separation of the flange from the web [3]. An approximate method to determine the local buckling critical stress ($\sigma_{cr,Local}$) has been proposed by Kollar [14]. For a wall that is simply supported and free at its edges under uniform compressive stress, the following equation may be used,

$$(\sigma_{free}^{ss})_{cr,Local} = \frac{\pi^2}{t_p \left(\frac{b_p}{2}\right)^2} \left[D_L \left(\frac{b_p/2}{a}\right)^2 + \frac{12}{\pi^2} D_S \right] \quad (4)$$

where t_p is the plate thickness, b_p is the plate width, D_L is the flexural rigidity in the longitudinal direction, a is the half-wave length and D_S is the shear rigidity.

For a wall that is simply supported along both edges under uniform compressive stress, the following equation may be used,

$$(\sigma_{ss}^{ss})_{cr,Local} = \frac{\pi^2}{t_p b_p^2} (\sqrt{D_L D_T} + D_{LT} + 2D_S) \quad (5)$$

where D_T is the flexural rigidity in the transverse direction and D_{LT} is the coupling flexural rigidity.

For a wall that is simply supported along both edges under linearly varying compressive stress, the following equation may be used,

$$(\sigma_{ss}^{ss})_{cr,Local} = \frac{\pi^2}{t_p a_p^2} (13,9\sqrt{D_L D_T} + 11,1D_{LT} + 22,2D_S) \quad (6)$$

The consideration of a free/simply supported flange is known to be an overly conservative assumption. To take into account the elastic restriction of web-flange junction, the following equation may be used,

$$\sigma_{cr,Local,f} = \frac{1}{(b_f/2)^2 t_f} \left(7 \sqrt{\frac{D_L D_T}{1 + 4,12\zeta}} + 12D_S \right) \quad (7)$$

The shear modulus (G_{LT}) is not often reported by manufacturers. In these cases, an approximate method proposed by the Structural Plastics Design Manual [9] may be used. The local buckling critical stress is given by the equation,

$$\sigma_{cr,Local}^{Approx} = \frac{\pi^2 t_f^2}{(b_f/2)^2} \left[\left(0,45 + \frac{b_f^2}{4a^2} \right) \frac{\sqrt{E_L E_T}}{12(1 - \nu_L \nu_T)} \right] \quad (8)$$

6. SHORT-COLUMNS FULL-SCALE EXPERIMENTAL TEST

6.1. OBJECTIVES AND PROCEDURE

To analyze the structural behavior of the pultruded profiles studied, four short-columns were tested under axial compression. The critical load (P_{cr}), the ultimate load (P_u), the maximum axial shortening (ΔL_{max}) and the longitudinal elastic modulus under compression (E) were obtained. Experimental results were then compared to analytic values.

The columns were tested with 60 cm nominal free length. At each end of the column, the profile was embedded in a 30x20x3 cm³ epoxy resin plate. This procedure was conducted to guarantee that the end sections were rotationally restrained and had no relative displacements.

Five strain gauges were bonded at mid-height of one column (column 2) in order to obtain the full-section longitudinal elastic modulus under compression (Figure 7).

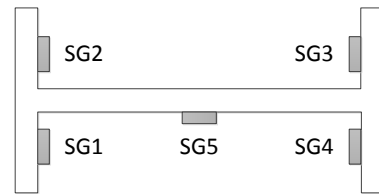


Figure 7. Strain gauges' disposition

Load was applied concentrically by a 3000 kN capacity universal testing machine. Plates with a 60 mm thickness were disposed at both ends so that the load was applied uniformly. To avoid stresses due to cut imperfections, a spherical hinge was used in the top end.

Axial shortening was measured by six displacement transducers (three at each end). Two additional displacement transducers were used to measure the lateral displacement of the web and one of the flanges at 15 cm from the top end (Figure 8).

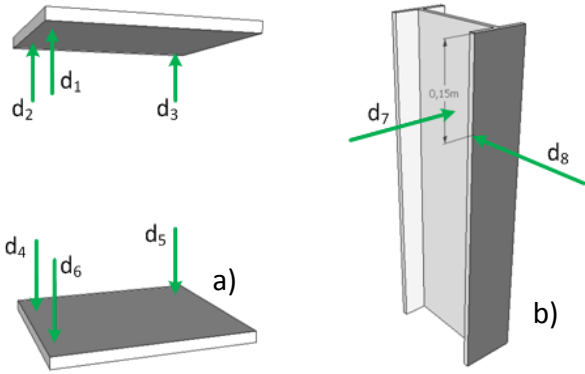


Figure 8. (a) Axial shortening transducers and (b) lateral deflection transducers

During each test, the strains, displacements and the applied load were recorded at a frequency of 1 Hz by a computer-controlled data-logger system. The test schematic representation is presented in Figure 9.

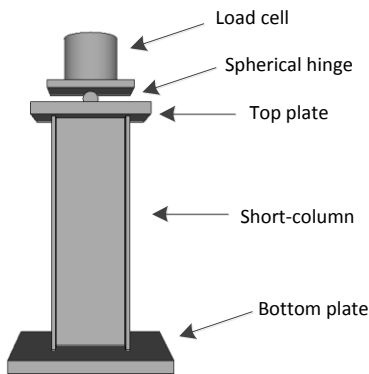


Figure 9. Short-column test schematic representation

6.2. ANALYSIS OF RESULTS

A significant adjustment phase was registered on the load-displacement curve of each column testing. The corrected load-displacement curves are presented in Figure 10.

The ultimate load (F_u) and maximum axial shortening (ΔL_{max}) of each short-column test are presented in Table 4.

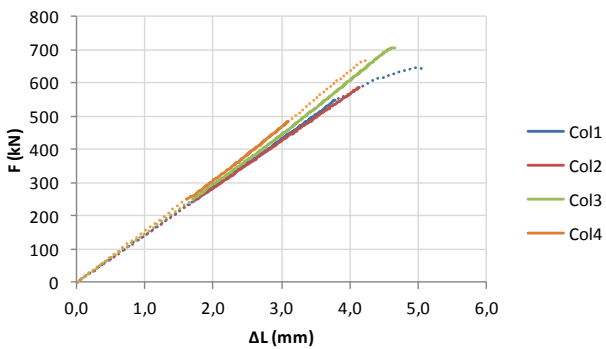


Figure 10. Load against axial shortening

Table 4. Ultimate load and maximum axial shortening

Column	F_u (kN)	ΔL_{max} (mm)
1	644,35	5,07
2	587,87	4,14
3	706,90	4,65
4	666,41	4,24
Average	651,41	4,53
Stand. Dev.	49,65	0,43
Variation	7,62%	9,39%

Despite the reduced variation percentages on both parameters, two different types of buckling were observed. Columns 1, 2 and 4 buckled with two half-waves along their length. Column 3 buckled with one half-wave along its length. Both buckling modes are shown in Figure 11.

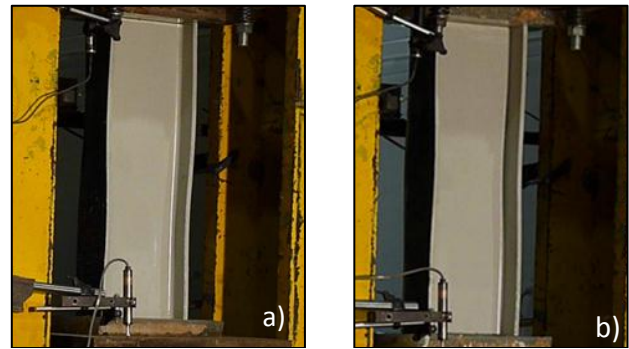


Figure 11. Buckling modes with (a) two and (b) one half-waves

Failure occurred with the separation of one or both flanges from the web, followed by delamination of both CFRP sheets (Figure 12).



Figure 12. Failure mode with tearing of flanges from the web

The measured lateral displacements on each test are presented in Figures 13, 14, 15 and 16. The web displacement is shown in blue and the flange displacement is shown in red.

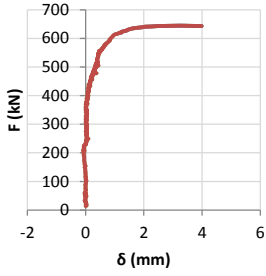


Figure 13. Lateral displacement on column 1

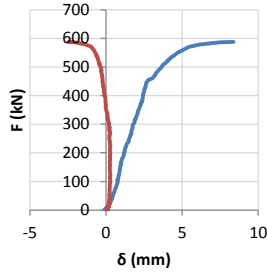


Figure 14. Lateral displacement on column 2

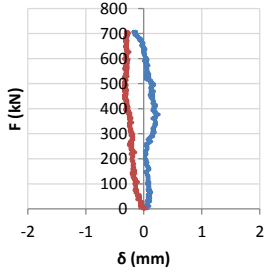


Figure 15. Lateral displacement on column 3

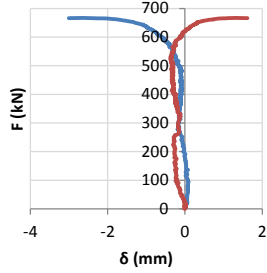


Figure 16. Lateral displacement on column 4

Figure 14 shows a linear evolution of the lateral web displacement which is a consequence of eccentrically applied load resultant from cut imperfections. Figure 15 shows no significant displacements because the measured section was near an inflection point of the buckling mode.

Critical loads were determined using an approximate method. The critical load was defined as the intersection of the load axis and a trend line of the final phase of the load against lateral displacement for each test (Figure 17).

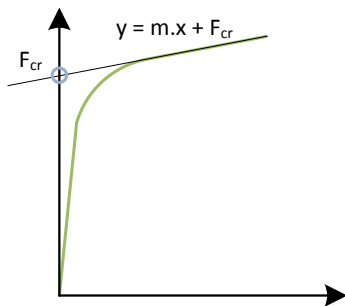


Figure 17. Critical load determination

The measured displacements of column 3 are near an inflection point of the buckling mode, therefore it was not possible to determine the critical load of the referred column. The remaining critical loads are presented in Table 5.

Table 5. Local buckling critical loads

Column	F_{cr} (kN)	F_u/F_{cr}
1	616,5	1,045
2	535,8	1,097
4	635,5	1,059
Average	595,9	1,067
Stand. Dev.	52,9	0,027
Variation	8,88%	2,52%

Column 2 was subjected to combined bending and axial compression. To determine the longitudinal elastic modulus (E), bending and compressive strains had to be considered separately (Figure 18). The section curvature (χ) was determined and it is presented in Figure 19.

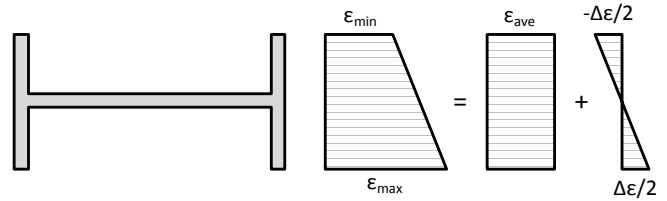


Figure 18. Influence of axial compression and bending in the section strain

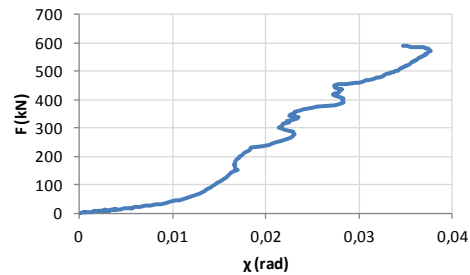


Figure 19. Load against curvature on column 2

The longitudinal elastic modulus (E) was defined as the slope of the following equation,

$$\sigma = \frac{F}{A} = E(\epsilon_{max} - \chi z) \quad (9)$$

where σ is the longitudinal stress at the bending neutral axis, F is the applied load, A is the cross-section area, ϵ_{max} is the maximum section strain and z is the distance from the bending neutral axis to the flange border ($z = 0,05$ m).

Figure 20 shows the trend line of equation (9) between 25 and 50 MPa.

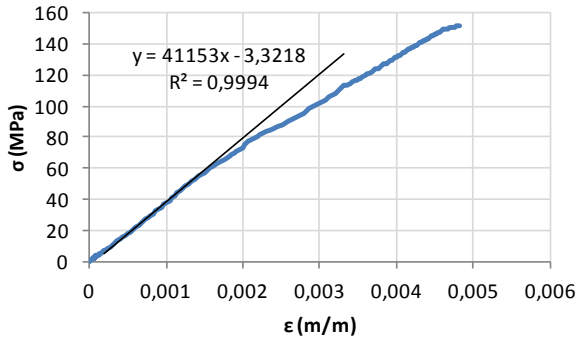


Figure 20. Stress against strain on column 2

The determined longitudinal elastic modulus under compression was **41,15 GPa**.

6.3. DISCUSSION AND CONCLUDING REMARKS

The experimental local buckling critical stress was compared to the analytical values obtained using equations (4), (7) and (8). The experimental local buckling critical stress ($\sigma_{f,cr,Local}$) was obtained using the following equation,

$$\sigma_{f,cr,Local} = \frac{P_{cr,Local} E_f}{(E_f A_f + E_w A_w)} \quad (10)$$

where $P_{cr,Local}$ is the critical load, E_f is the flanges longitudinal elastic modulus, A_f is the flanges area, E_w is the web longitudinal elastic modulus and A_w is the web area.

Critical stresses of the columns 1, 2 and 4 are presented in Table 6.

Table 6. Local buckling critical stress

Column	$\sigma_{f,cr,Local}$ (MPa)
1	200,8
2	174,5
4	207,0

Using K ollar's equation which considers a free/simply supported flange, a local buckling critical stress of **223,3 MPa** is obtained.

Using K ollar's equation which considers the web-flange junction elastic restriction, a local buckling critical stress of **184,0 MPa** is obtained.

Using the Structural Plastics Design Manual approximate method equation, a local buckling critical stress of **389,3 MPa** is obtained.

The equation which gave a better approximation was equation (7), considering the elastic restriction of the web-flange junction, with an average percent error of 8,9%.

Using the obtained longitudinal elastic modulus under compression ($E = 41,15$ GPa) on equation (1), the axial shortening is **4,05 mm**. The percent error between the analytical and the experimental axial shortening was 11,94%.

7. BEAM FULL-SCALE EXPERIMENTAL TEST

7.1. OBJECTIVES AND PROCEDURE

To analyze the structural behavior of the pultruded profile studied, a simply supported beam under four-point bending was tested. The ultimate load (P_u), the maximum transverse deflection (δ_{max}) and the full-section elastic moduli (E and G) were determined and experimental results were then compared to analytical values.

Two types of tests were carried out:

- Serviceability behavior – several load/unload tests were carried out in order to obtain the elastic moduli (E and G) under bending;
- Ultimate behavior – study of the ultimate load as well as the failure mode.

The test span (L) was 4,0 m. The distance between load points (L_0) varied from 1,0 to 2,0 m for the elastic moduli determination stage. The distance between load points for the ultimate load determination stage was 1,40 m (approximately $L/3$). An auxiliary steel beam was used to distribute the applied load. The total beam length was 4,40 m.

Nine strain gauges were bonded at mid-span of the beam in order to obtain the full-section longitudinal elastic modulus (E) under bending (Figure 21).

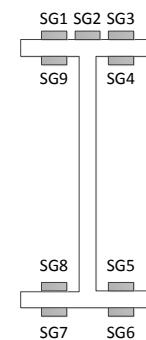


Figure 21. Strain gauges' disposition

The load was applied by a 600 kN capacity hydraulic jack and measured with a load cell with 100 kN capacity. Lateral bracing was required to avoid lateral-torsional buckling. The braced sections are shown in Figure 22.

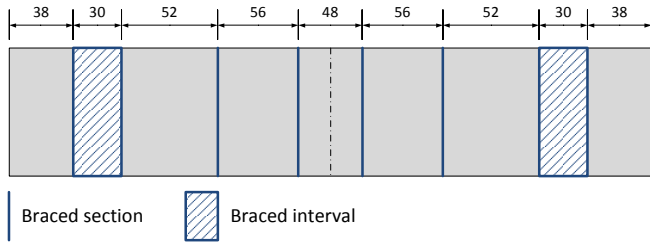


Figure 22. Lateral bracing on the beam test (measures in cm)

Transverse deflection was measured by three displacement transducers placed under the mid-span section and two other sections distanced from the mid-span by 0,70 m. Two additional displacement transducers were used to measure section displacements due to buckling.

During each test, strains, displacements and applied load were recorded at a frequency of 10 Hz by a computer-controlled data-logger system. The test schematic representation is presented in Figure 23.

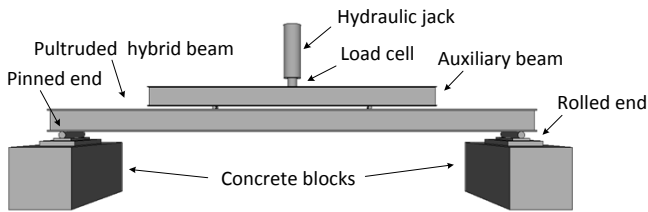


Figure 23. Short-column test schematic representation

7.2. ELASTIC MODULI DETERMINATION

Having measured the transverse displacements it is possible to determine the full-section elastic moduli using the Timoshenko beam theory. Equations (2) and (3) may be rearranged in the following equations,

$$-\frac{2\delta(z)}{Pz} = \frac{1}{EI} \left(-\frac{z^2}{12} - \frac{(L-L_0)^2}{16} + \frac{L(L-L_0)}{8} \right) + \frac{1}{KGA} \quad (11)$$

$$\rightarrow z < \frac{L-L_0}{2}$$

$$-\frac{4\delta(z)}{P(L-L_0)} = \frac{1}{EI} \left(-\frac{z^2}{8} + \frac{Lz}{8} - \frac{(L-L_0)^2}{96} \right) + \frac{1}{KGA} \rightarrow z > \frac{L-L_0}{2} \quad (12)$$

A scatter was made with the measured $P-\delta(z)$ values. With the scatter trend line, the values of $\frac{1}{EI}$ (slope) and $\frac{1}{KGA}$ (vertical axis intercept) can be obtained. The scatter and the respective trend line are presented in Figure 24.

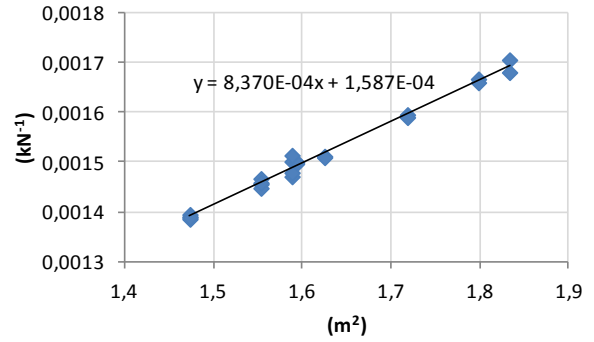


Figure 24. Elastic moduli determination scatter

The elastic moduli (E and G) were then determined and are presented in Table 7.

Table 7. Elastic moduli determination

$1/EI$ ($kN^{-1}m^{-2}$)	EI (kNm^2)	E (GPa)
$8,37 \times 10^{-4}$	1194,74	50,78
$1/KGA$ (kN^{-1})	KGA (kN)	G (GPa)
$1,587 \times 10^{-4}$	6301,29	3,92

7.3. ANALYSIS OF RESULTS

The load-displacement curves are shown in Figure 1 (d_1 is the mid-span displacement; d_2 and d_3 are the displacements under the load application points). Delamination of the upper flange CFRP sheet occurred for an applied load of 29,82 kN.

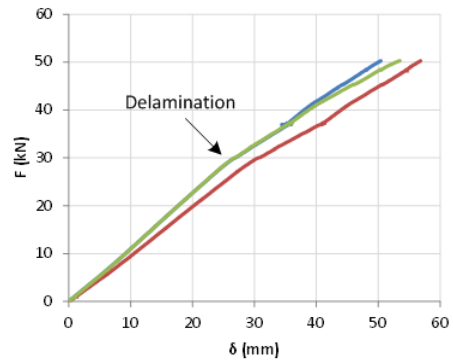


Figure 25. Load against transverse deflection

With a trend line of the load-displacement curve before the CFRP sheet delamination it was possible to obtain the apparent longitudinal modulus ($E_a = 47,13$ GPa) and the shear deformability influence (9,94%).

A significant stiffness loss was verified after the delamination (about 31%). The global transverse deflection before failure is shown in Figure 26.



Figure 26. Global transverse deflection on the brink of collapse

Failure occurred with web-flange separation as it usually occurs in local buckling phenomena. However, the lateral bracing system was considered inadequate since two steel props were laterally pulled when failure occurred. A combined global and local buckling mode may have occurred due to lack of lateral bracing rigidity.

The ultimate load was **50,41 kN**, with a maximum deflection of **56,81 mm**.

The lateral web displacement (blue) and the difference between displacements at the upper flange borders (red) are shown in Figure 27. Both measured displacements are consistent with lateral-torsional buckling (Figure 28). The load-curvature curve is shown in Figure 29.

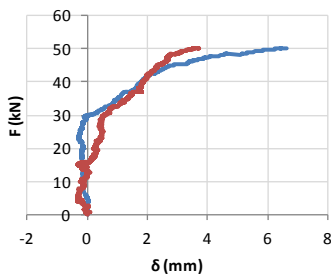


Figure 27. Beam section displacements

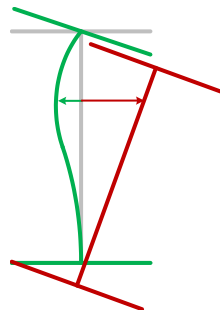


Figure 28. Local (green) and global (red) buckling

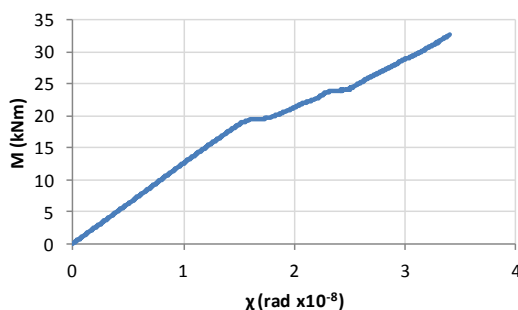


Figure 29. Load against curvature

7.4. DISCUSSION AND CONCLUDING REMARKS

The experimental local buckling critical stress was compared to the analytical values obtained using equations (4), (7) and (8). Due to the global buckling phenomenon and the impossibility to apply the Southwell plot, the analytical local buckling stresses were compared with the ultimate compressive stress on the upper flange ($\sigma_u = 144,0$ MPa).

Using K ollar's equation which considers a free/simply supported flange, a local buckling critical stress of **140,2 MPa** is obtained.

Using K ollar's equation which considers the web-flange junction elastic restriction, a local buckling critical stress of **195,7 MPa** is obtained.

Using the Structural Plastics Design Manual approximate method equation, a local buckling critical stress of **208,5 MPa** is obtained.

The equation which gave a better approximation was equation (4), considering a free/simply supported flange with a percent error of 3,4%. However, this equation is often considered to be over conservative.

A maximum deflection of **52,2 mm** is obtained using the Timoshenko beam theory with the elastic moduli determined in 7.2. The percentage error between experimental and analytical deflection was 8,1% but since this value does not consider the CFRP sheet delamination it is, naturally, a lower bound of the experimental value.

8. SHORT-COLUMN FE NUMERICAL MODELING

8.1. PRELIMINARY FE MODEL

FE models of the tested columns were developed using the *ABAQUS* program [15]. Shell elements with four nodes were used. Material was considered to be composite, laminate and elastic. Properties determined in the mechanical characterization were used in this stage. A 23-node section as shown in Figure 30 was used. The column length was considered to be 60 cm.

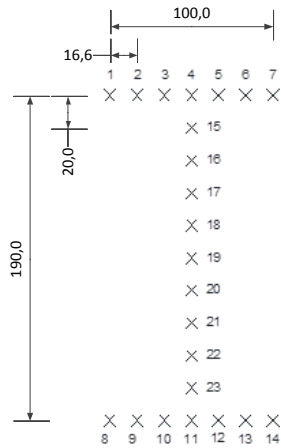


Figure 30. Profile section of the FE models (in mm)

The Tsai-Hill failure criterion was used. This failure criterion considers the interaction between material strengths and is given by the following equation,

$$I_F = \frac{\sigma_{11}^2}{X^2} - \frac{\sigma_{11}\sigma_{22}}{X^2} + \frac{\sigma_{22}^2}{Y^2} + \frac{\sigma_{12}^2}{S^2} < 1,0 \quad (13)$$

where σ_{11} is the longitudinal stress, σ_{22} is the transverse stress, σ_{12} is the shear stress, X is the longitudinal strength, Y is the transverse strength and S is the shear strength. The Tsai-Hill criterion indicates the first failure point of the structural element but not the collapse.

A **linear buckling analysis** was performed in order to obtain the critical load (P_{cr}), the number of half-waves (n_{hw}) and the half-wave length (L_{hw}) of the first three buckling modes. Results are shown in Table 8.

Table 8. Buckling analysis results

Buckling mode	P_{cr} (kN)	L_{hw} (cm)	n_{hw}
1 st	763,49	20,0	2
2 nd	809,78	20,3	1
3 rd	1102,11	14,0	3

The comparison between numerical and experimental critical loads leads to a difference of 128 kN (17%). With these results it is necessary to calibrate the model with the results presented on the full-scale short-column testing.

A **non-linear analysis** was then carried out in order to obtain load-displacement data until initial failure occurs. For an initial imperfection according to the first buckling mode

(2 half-waves – 2HW), an initial failure load (P_{if}) of 789,34 kN and an axial shortening of 2,82 mm were determined. The load-displacement curve and the deformed shape at the initial failure are shown in Figures 31 and 32.

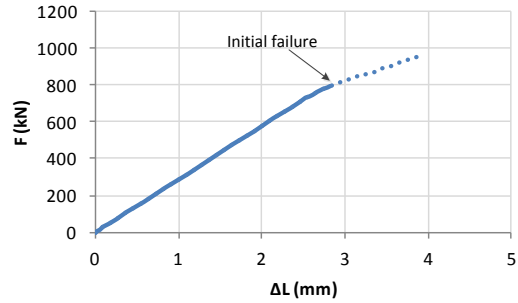


Figure 31. Load against displacement

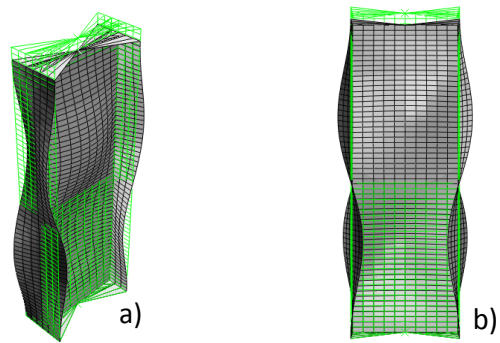


Figure 32. (a) Perspective and (b) front view of the deformed shape at initial failure (scaled 8x)

The stresses (σ_{11} , σ_{22} and τ_{12}) at initial failure are shown in Figure 33. The elements on which initial failure occurs are shown in Figure 34.

The maximum stresses at the elements on which initial failure occurs are presented in Table 9.

Table 9. Maximum stresses and strengths (2HW)

	Stress (MPa)	Strength (MPa)	Percent
σ_{11}	154,1	495,1	31,1%
σ_{22}	0,991	130,1	0,8%
τ_{12}	29,12	30,59	95,2%

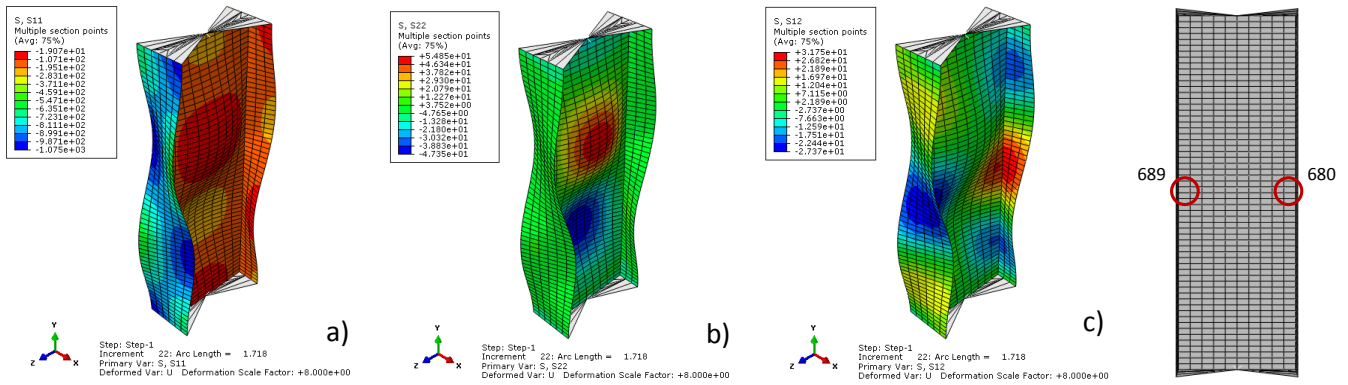


Figure 33. (a) Longitudinal stress, (b) transverse stress and (c) shear stress (scale colour in MPa)

Figure 34. Initial failure elements

As presented in Table 9, the Tsai-Hill criterion at failure was very dependent of the shear stress. Both longitudinal and transverse stresses were clearly lower than their strengths.

A similar non-linear analysis was conducted for an initial imperfection according to the second buckling mode (1 half-wave – 1HW). In fact, the initial failure load was slightly higher (804,72 kN) but when the Tsai-Hill criterion was reached the buckling mode exhibited 2 half-waves. The maximum stresses at the elements on which initial failure occurs are presented on Table 10.

Table 10. Maximum stresses and strengths (1HW)

	Stress (MPa)	Strength (MPa)	Percent
σ_{11}	155,94	495,1	31,5%
σ_{22}	2,965	130,1	2,3%
τ_{12}	29,01	30,59	94,8%

Once again shear stress was almost 95% of its strength and both longitudinal and transverse stresses were clearly lower than their strengths.

8.2. CALIBRATION

Calibration was carried out varying the elastic moduli (E and G), in order to obtain more approximate results between numerical analysis and experimental testing. Critical load (P_{cr}) and load-displacement slope (F- Δ L) were the chosen parameters to calibrate. Results are presented in Table 11. The variations of the elastic moduli are presented in Table 12.

Table 11. Calibration parameters

	F- Δ L (kN/mm)	P_{cr} (kN)
Experimental	146,9	626,0
Numerical	148,3	631,8
Difference	0,95%	0,93%

Table 12. Calibrated elastic moduli

	$E_{L,GFRP}$ (GPa)	$E_{L,CFRP}$ (GPa)	G_{LT} (GPa)
Preliminary model	32,81	181,85	3,73
Calibrated model	16,41	90,93	4,10
Difference	50%	50%	10%

The high decrease of the longitudinal elastic moduli was not expected. Some factors which may explain such decrease are (i) the use of the longitudinal elastic modulus in tension in preliminary modeling, (ii) local bearing at end sections, (iii) an inadequate column length or (iv) geometrical imperfections. Even with the combination of all referred factors, a reduction of 50% of the longitudinal modulus is very high and should be pointed for further research.

For an initial imperfection according to the first buckling mode (2HW) the load-displacement numerical and experimental curves are shown in Figure 35.

The comparison between numerical and experimental results obtained for columns 1 and 4 is presented in Table 13.

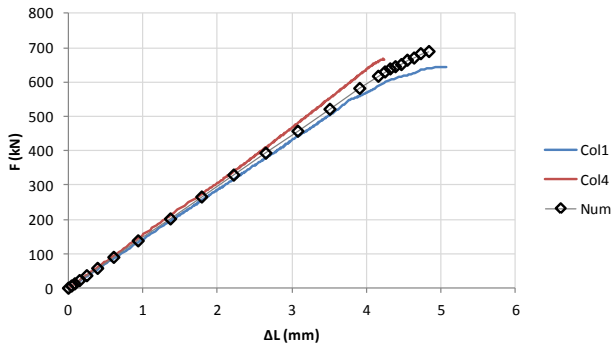


Figure 35. Load against axial shortening (experimental versus numerical results)

Table 13. Comparison between calibrated model numerical and experimental results (2HW)

	P_u / P_{if} (kN)	$\Delta L_{max}; \Delta L_{max,num}$ (mm)
Numerical	655,52	4,49
Column 1	644,35	5,07
Perc. Diff.	1,70%	12,92%
Column 4	666,54	4,24
Perc. Diff.	1,68%	5,57%

Both the initial failure load and the maximum numerical axial shortening are in between columns 1 and 4 experimental results with reduced percentage differences. The web and flange lateral displacements comparison is presented on Figure 36.

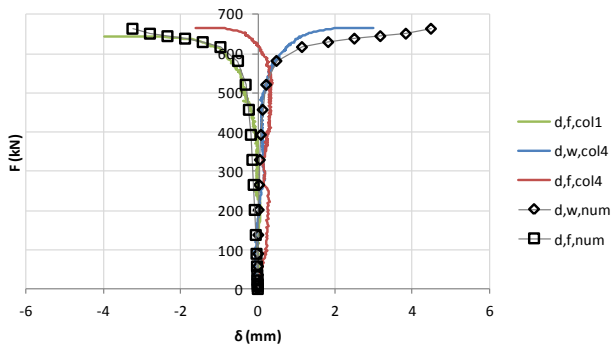


Figure 36. Web and flanges lateral displacements (experimental versus numerical results)

Once again, at initial failure, the shear stress was very close to its strength (98,3%) and both longitudinal and transverse stresses were clearly lower than their strengths (25,5% and 0,4% respectively).

A similar analysis was conducted for an initial imperfection according to the second buckling mode (1HW). The exper-

imental versus numerical results comparison is presented on Table 14.

Table 14. Comparison between calibrated model numerical and experimental results (1HW)

	P_u / P_{if} (kN)	$\Delta L_{max} / \Delta L_{max,num}$ (mm)
Numerical	695,33	4,74
Column 3	706,90	4,65
Perc. Diff.	1,66%	1,90%

The column deformed shape at initial failure is shown on Figure 37. The finite elements on which the Tsai-Hill criterion was first reached were the 528 and the 519 (Figure 38).

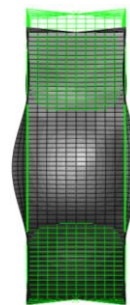


Figure 37. Deformed shape at initial failure

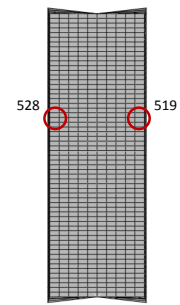


Figure 38. Initial failure elements

Shear stress was once again determinant reaching 98,5% of its strength at initial failure.

8.3. PARAMETRIC STUDIES

In this section, the influence of the profile shape and length on the local buckling critical load is discussed. Parametric studies were conducted varying the column length between 60 and 300 cm for a narrow flange (NF) shaped profile (200x100x10 mm) and between 60 and 600 cm for a wide flange (WF) shaped profile (200x200x10 mm). Results are shown in Figures 39 and 40.

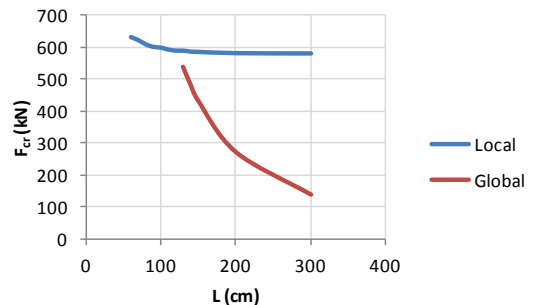


Figure 39. Local and global buckling curves (NF-profile)

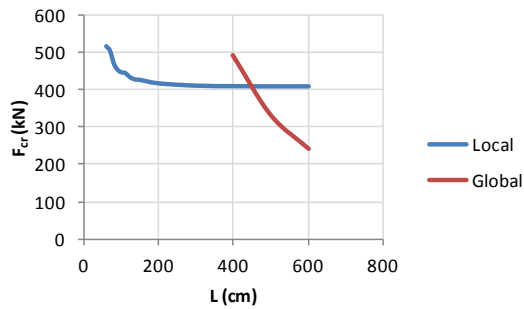


Figure 40. Local and global buckling curves (WF-profile)

For the NF-profile the “critical” length was about 120 cm. For the WF-profile the “critical” length was about 450 cm. Local buckling critical load was higher on the NF-profile (about 600 kN) than on the WF-profile (about 400 kN).

With the presented analysis and having the critical load as the only criterion to choose a profile shape, the NF-profile is recommended for columns with lengths up to 150 cm. For superior lengths the WF-profile is recommended (Figure 41).

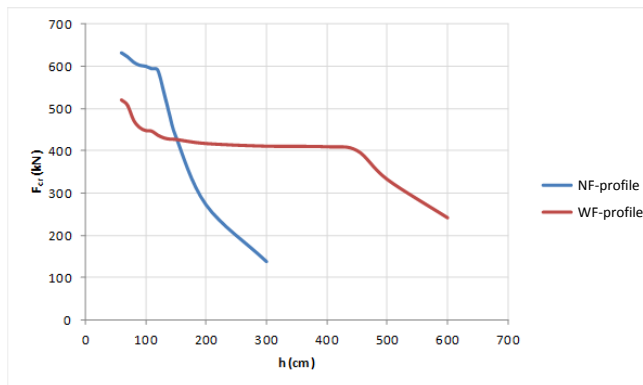


Figure 41. Comparison between NF-profile and WF-profile critical loads

9. BEAM FE NUMERICAL MODELING

9.1. PRELIMINARY FE MODEL

The profile section and failure criterion used in 8.1 were also used in this section. The beam dimensions as well as

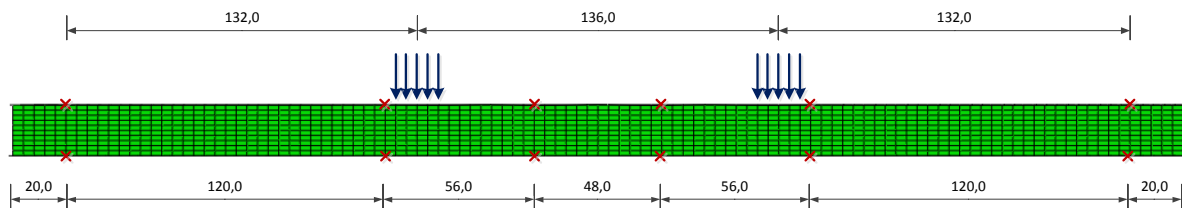


Figure 42. Beam dimensions, load points and laterally braced points

the load points and the laterally braced nodes are shown in Figure 42.

A **linear buckling analysis** was performed in order to obtain the critical load (P_{cr}), the number of half-waves (n_{hw}) and the half-wave length (L_{hw}) of the first three buckling modes. Results are presented in Table 15.

Table 15. Buckling analysis results

Buckling mode	P_{cr} (kN)	L_{hw} (cm)	n_{hw}
1 st	124,87	27,4	8
2 nd	125,31	20,2	9
3 rd	129,48	20,3	10

It is not possible to compare numerical and experimental results since (i) the upper flange CFRP sheet delaminated and (ii) a lateral-torsional buckling mode occurred. Numerical and experimental results comparison will only be presented for the calibrated FE model.

A **non-linear analysis** was carried out in order to obtain load-displacement data until initial failure occurs. For an initial imperfection according to the first buckling mode (8HW), an initial failure load of 115,89 kN and mid-span transverse deflection of 117,8 mm were determined. The load-displacement curve and the deformed shape at the initial failure load are shown in Figures 43 and 44.

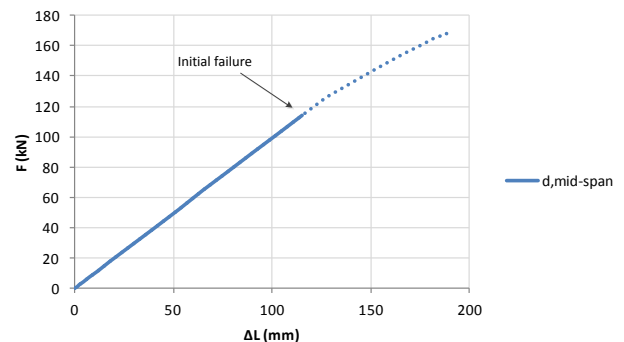


Figure 43. Load against displacement

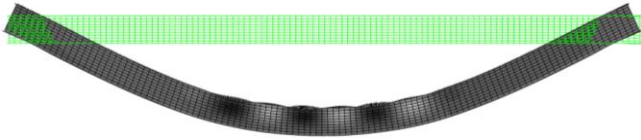


Figure 44. Deformed shape at initial failure (scaled 8x)

Initial failure occurs on elements 795 and the 1738 as shown in Figure 45.



Figure 45. Initial failure elements

The maximum stresses of the elements on which initial failure occurs are presented in Table 16.

Table 16. Maximum stresses and strengths

	Stress (MPa)	Strength (MPa)	Percent
σ_{11}	179,11	495,1	36,2%
σ_{22}	27,84	130,1	21,4%
τ_{12}	30,07	30,59	98,3%

As presented on Table 16, the Tsai-Hill criterion at failure was very dependent of the shear stress (98,3% of its strength). Both longitudinal and transverse stresses are clearly lower than their strengths.

9.2. CALIBRATION

In the calibration stage two different FE models were developed, due to the upper flange CFRP sheet delamination (one with and one without CFRP sheet on the upper flange).

Once lateral-torsional buckling occurred it was necessary to model the lateral bracing in a different way. The solution found was the use of beam elements with axial elastic stiffness (k) instead of a displacement restriction at the braced nodes (Figure 46).

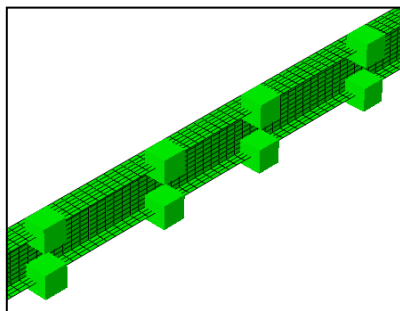


Figure 46. Lateral bracing system modeling

Calibration was carried out varying the elastic moduli (E and G), the initial imperfection and the elastic bracing stiffness (k) in order to obtain more approximate results between numerical analysis and experimental testing. The initial load displacement slope ($F-\delta_{mid-span}$) and the section displacements were the chosen parameters to calibrate. Results are presented in Table 17. The variations of the elastic moduli, initial imperfection and elastic bracing stiffness are presented in Table 18.

Table 17. Calibration parameters

	$F-\delta_{mid-span}$ (kN/mm)
Experimental	1,0171
Numerical	1,0105
Difference	0,65%

Table 18. Calibrated elastic moduli, initial imperfection and elastic bracing stiffness

	$E_{L,GFRP}$ (GPa)	$E_{L,CFRP}$ (GPa)	G_{LT} (GPa)	τ_u (MPa)
Preliminary model	32,81	181,85	3,92	30,59
Calibrated model	36,75	203,67	4,39	21,00
Difference	12%	12%	12%	32%
Initial imperfection	2 mm			
k (kN/m)	250			

The most significant variation was the reduction of the shear strength (32%). Such fact may be explained by a possible difference between the fiber configuration in the web-flange junction and in the web. The deformed shape of the first buckling mode was obtained by running a buckling analysis in the calibrated model (Figure 47).



Figure 47. First buckling mode of the calibrated FE model

The load-displacement numerical and experimental curves for an initial imperfection according to the first buckling mode are shown in Figure 48.

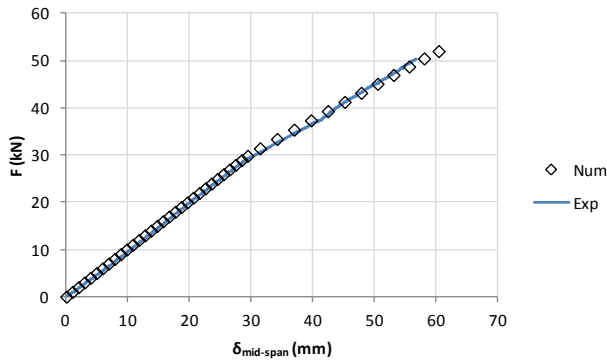


Figure 48. Load against mid-span transverse deflection (experimental versus numerical)

The comparison between numerical and experimental results is presented in Table 19.

Table 19. Comparison between calibrated model numerical and experimental results

	P_u / P_{if} (kN)	$\delta_{mid-span,max} / \delta_{midspan,max,num}$ (mm)
Numerical	52,01	60,45
Ensaio	50,29	56,81
Perc. Diff.	3,30%	6,02%

Both the initial failure load and the maximum transverse deflection have had reduced percentage differences. The web and flange displacements comparison is presented in Figure 49.

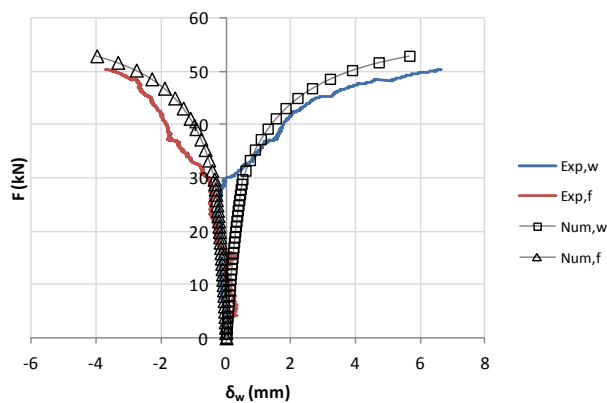


Figure 49. Web and flanges displacements (experimental versus numerical results)

The finite elements on which the Tsai-Hill criterion was first reached were 1186 and the 1324. They are located near the inflection point of the beam's deformed configuration (Figure 50).

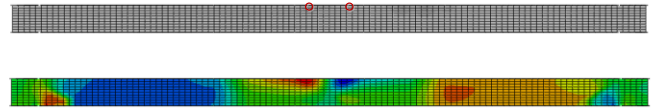


Figure 50. Initial elements failure

Shear stress was once again determinant reaching 98,2% of its strength.

9.3. SHAPE INFLUENCE

In this section, the influence of the profile shape on both the local buckling critical load and the initial failure load was studied.

Delamination occurred in the material characterization stage for a strain of 0,62% and in the full-scale beam test for a strain of 0,154%.

Since delamination was not expected in the full-scale beam test, four different models were developed, two for a NF-profile (with and without considering delamination) and two others for a WF-profile (also with and without considering delamination). Results of this parametric study are presented in Table 20.

Table 20. Parametric study results

Profile	Delaminated		Without delamination	
	P_{cr} (kN)	P_{if} (kN)	P_{cr} (kN)	P_{if} (kN)
NF	104,92	58,00	138,59	58,72
WF	51,94	53,64	78,24	62,63

As expected, critical buckling loads were considerably lower for the WF-profile (between 49% and 57% of the NF-profile critical load) due to the higher flange slenderness ratio (width to thickness).

The initial failure loads have had a low variation (6,3%) due to the strong dependency of the shear strength (which is the same in all models).

10. FINDINGS AND CONCLUSIONS

In this dissertation the structural behavior of a hybrid pultruded profile was studied. For this purpose experimental tests were carried out and FE models were developed. The following main conclusions are drawn from this study:

1. The determination of strengths and elastic moduli took place in the mechanical characterization stage. All values were in agreement with the values provided by the bibliographic references.

2. For serviceability limit states, both structural elements (columns and beam) may be analyzed with simple models using the uniaxial bar theory and the Timoshenko beam theory.
3. For the short-column testing, equation (7) gave a better approximation to the experimental local buckling critical stress, with an average percent error of 8,9%. This equation developed by Kollar considers the elastic restriction of the web-flange junction.
4. The four-point bending beam test may be repeated with an adequate lateral bracing to avoid lateral-torsional buckling.
5. In the short-column numerical calibration, the high decrease of the elastic moduli may be pointed for further research.
6. The performed parametric studies confirmed the higher sensitivity to local buckling of WF-profiles.
7. The interaction between the CFRP sheets and the GFRP reinforcement may be highlighted for further investigation and other flange hybridization patterns may be studied.
8. Global buckling as well as long-term deflection may be subjects of further research.

REFERENCES

- [1] P.M.V. Teixeira, *Análise e Dimensionamento de Perfis Pultrudidos de GFRP*, MSc Thesis in Civil Engineering, Instituto Superior Técnico, UTL, 2010.
- [2] J.R. Correia, *Glass fibre reinforced polymer (GFRP) pultruded profiles. structural behaviour of GFRP-concrete hybrid beams*, MSc Dissertation in Construction, Instituto Superior Técnico, UTL, 2004 (in Portuguese).
- [3] L.C. Bank, *Composites for construction: Structural design with FRP materials*. Wiley, Hoboken, N.J, 2006.
- [4] CEN, EN ISO 14125 *Fibre-reinforced plastic composites – Determination of flexural properties*, Brussels, 1998.
- [5] ASTM D2344/D 2344M-00 *Standard Test for Short-Beam Strength of polymer Matrix Composite Materials and their Laminates*, West Conshohocken, PA, 2006.
- [6] ASTM D 695-02 *Standard Test Method for Compressive Properties of Rigid Plastics*, West Conshohocken, PA, 2006.
- [7] CEN, ISO 527-4 *Determination of tensile properties – Part 4: Test conditions for isotropic and orthotropic fibre-reinforced plastic composites*, Brussels, 1997.
- [8] CEN, ISO 527-5 *Determination of tensile properties – Part 5: Test conditions for unidirectional fibre-reinforced plastic composites*, Brussels, 1997.
- [9] ASCE, *Structural Plastics Design Manual*, No. 63, 2002.
- [10] J.L. Clarke, *Eurocomp Design Code and Handbook*, E&FN Spon, 1996.
- [11] L.C. Bank, M. Nadipelli e T.R. Gentry, *Local Buckling and Failure of Pultruded fiber-Reinforced Plastic Beams*, Journal of Engineering Materials and Technology, Vol. 116, No. 2, pp. 233-238, 1994.
- [12] J.T. Mottram, *Determination of critical load for flange buckling in concentrically loaded pultruded columns*, Composites: Part B, Vol. 35, No. 1, pp. 33-47, 2004.
- [13] G.J. Turvey e Y. Zhang, *A computational and experimental analysis of the buckling, postbuckling and initial failure of pultruded GRP columns*, Computers and Structures, Vol. 84, No. 22-23, pp. 1527-1537, 2006.
- [14] L.P. Kollár, *Local buckling of fiber reinforced plastic composite structural members with open and closed cross sections*, Journal of Composites for Construction, Vol.129, No.11, pp. 1503-1513, 2003.
- [15] Simulia, *Abaqus Standard: User's Manual*, Versão 6.5, 2004.